EDGE ARTICLE

Simultaneously enhancing the planarity and electron-donating capability of donors for through-space charge transfer TADF towards deep-red emission†

Xiu-Fang Song,‡[ab] Chenglin Jiang,‡[a] Nengquan Li, [iD] [a] Jingsheng Miao,[a] Kai Li [iD] *[a] and Chuluo Yang [iD] *[a]

Through-space charge transfer (TSCT) has been proven effective for designing thermally activated delayed fluorescence (TADF) emitters due to the separation of the frontier molecular orbitals. Although tuning of the interaction between the donor and acceptor by controlling the conformation is known to be crucial for the photophysical properties of TSCT excited states, it remains a challenge to realize efficient red and deep-red emissions. Herein, we designed two TSCT molecules, namely **TPXZ-QX** and **TPXZ-2QX**, by using oxygen-bridged triphenylamine (TPXZ) as the electron donor with enhanced planarity and electron-donating capability. With a face-to-face orientation of the donor and acceptor segments and close $\pi-\pi$ contacts, the new emitters have strong intramolecular noncovalent donor–acceptor interactions. The emissions of **TPXZ-QX** and **TPXZ-2QX** in doped thin films lie in the red ($\lambda_{max} = 632$ nm) to deep-red ($\lambda_{max} = 665$ nm) region. The photoluminescence quantum yields are 41% and 32% for **TPXZ-QX** and **TPXZ-2QX**, respectively. Organic light-emitting diodes (OLEDs) based on **TPXZ-QX** and **TPXZ-2QX** show external quantum efficiencies (EQEs) of up to 13.8% and 11.4%, respectively. This work indicates that the modulation of TSCT excited states based on strong intramolecular cofacial π-stacking interactions is a viable choice for the development of high-efficiency long-wavelength TADF emitters.

Introduction

Since the Adachi group reported a series of highly efficient thermally activated delayed fluorescence (TADF) emitters in 2012, purely organic molecules exhibiting TADF have emerged as the most appealing luminescent materials for organic light emitting diodes (OLEDs).[1–4] Compared with the fluorescent and phosphorescent emitters, TADF materials hold the combined advantages of 100% exciton utilization and low cost without using noble metals. A key step of TADF for harvesting the triplet excitons is the reverse intersystem crossing (RISC) from the lowest triplet excited state (T_1) to the lowest singlet excited state (S_1). To realize a fast RISC process, both a small energy gap

(ΔE_{ST}) between the S_1 and T_1 states and a strong spin–orbit coupling (SOC) effect are beneficial.[3,5–8] Considering the very small SOC value for pure organic molecules, a rapid RISC process can take place only when the ΔE_{ST} is small enough. In principle, ΔE_{ST} is in direct proportion to the exchange energy, which is related to the overlap of the wave functions of the highest occupied molecular orbital (HOMO) and the lowest unoccupied molecular orbital (LUMO). Therefore, a general consideration for design of TADF molecules is to spatially separate the electron-donor and electron-acceptor, which dominate the HOMO and LUMO distributions, respectively.[9] To this end, the donor and acceptor groups in most of the TADF molecules are linked by a π-conjugated linker to have a twisted geometry. In addition, it has also been shown that the properly disposed donor and acceptor segments, between which the π-conjugation is interrupted by σ-linker, can also exhibit TADF properties.[10]

Among the various approaches for constructing TADF molecules, intramolecular through-space charge transfer (TSCT) provides an appealing choice. This type of molecule has intrinsically small ΔE_{ST} values because of the diminished through-bond conjugation between the donor and acceptor segments. A pioneering work using the TSCT tactic for designing TADF materials was reported by Wang *et al.* in

[a]Shenzhen Key Laboratory of New Information Display and Storage Materials, College of Materials Science and Engineering, Shenzhen University, Shenzhen 518055, China. E-mail: kaili@szu.edu.cn; clyang@szu.edu.cn

[b]College of Physics and Optoelectronic Engineering, Shenzhen University, Shenzhen 518060, China

† Electronic supplementary information (ESI) available: Single crystal analysis, synthetic and characterization details, computational details and supplementary NMR spectra of the two molecules. CCDC 2223327 and 2223328. For ESI and crystallographic data in CIF or other electronic format see DOI: https://doi.org/10.1039/d3sc04264b

‡ Xiu-Fang Song and Chenglin Jiang contributed equally.

polymers.[11] In the meantime, Swager *et al.* reported the TADF properties from TSCT excited states of U-shaped donor–acceptor molecules in which the donor and acceptor planes are bridged by 9,9-dimethylxanthene.[12] Whereas, the photoluminescence quantum yields (PLQYs) of these U-shaped molecules are only moderate, likely due to the structural flexibility. Recently, tremendous progress has been made in the emission efficiencies of TSCT-TADF emitters. For example, Jiang *et al.* reported space-confined donor and acceptor alignment for TADF emissions with photoluminescence quantum yields (PLQYs) close to unity, benefiting from the fast RISC process and suppressed nonradiative decay.[13–15] Wang *et al.* realized efficient TADF from a series of dendrimers in which an array of donors and acceptors are linked alternatively.[16,17] Obviously, the distance and orientation of the donor and acceptor groups play crucial roles in dictating the photoluminescence properties of TSCT excited states. With the prerequisite small ΔE_{ST} values, the radiative decay rates of TSCT states are of equal importance, and are associated with the donor–acceptor electronic communication. Following this consideration, we have proposed a cofacial donor–acceptor alignment for maximizing the donor–acceptor interactions. Indeed, green and red TADF emissions with up to almost unity PLQYs have been developed for both double-decker and sandwich type molecules.[18–20] Duan *et al.* reported high-efficiency blue TSCT-TADF emitters which have high radiative decay rates of S_1 states of up to 10^7 s^{-1} arising from a very tight donor–acceptor alignment.[21] The manipulation of the distance and orientation of the donor and acceptor has led to a number of highly efficient TSCT-TADF emitters.[22–26]

In contrast with the various reports on green and blue TSCT-TADF emitters, there are only a few red and deep-red TADF emitters featuring TSCT excited states.[20,27,28] Presumably, it is difficult to simultaneously modify the geometric and electronic structures of the donor/acceptor for red-shifting the emission spectrum as well as maintaining appreciable PLQYs. Indeed, the choice of suitable donor moieties with both a flat geometry and strong electron-donating capability has been very limited. On the other hand, despite the significance of intramolecular noncovalent interactions in determining the photophysical properties of TSCT excited states, the quantitative analysis of the donor–acceptor interactions in terms of stabilizing energy for the TSCT molecules has not been performed. Herein, we designed and synthesized two red and deep-red TSCT-TADF molecules, namely **TPXZ-QX** and **TPXZ-2QX**, using oxygen-bridged triphenylamine (TPXZ) as the donor (Scheme 1). Planar dibenzo[*a,c*]phenazine (QX) is used as the acceptor. Their structures have been characterized by single-crystal X-ray diffraction analysis which suggests a face-to-face orientation of the donor and acceptor and strong donor–acceptor interactions. The intramolecular noncovalent interactions have been analyzed using intramolecular symmetry adapted perturbation theory (I-SAPT) in Psi4 code.[29,30] **TPXZ-QX** and **TPXZ-2QX** exhibit TSCT-TADF emissions (λ_{em} = 637–662) with PLQYs of 41% and 32% in doped thin films, respectively. The emitters deliver external quantum efficiencies (EQEs) of up to 13.8% and 11.4% for red and deep-red OLEDs.

Results and discussion

Design, synthesis, and structures

The structures and synthetic routes of **TPXZ-QX** and **TPXZ-2QX** are shown in Scheme 1. The syntheses of intermediates CQX and C2QX have been described previously.[20] For these two molecules, the donor moiety, TPXZ, has much improved planarity arising from the incorporation of three bridging O atoms into the skeleton.[31,32] In addition, the presence of multiple O atoms bestows the donor with a strong electron-donating capability. Both the geometrical and electronic features are beneficial for the design of TSCT-TADF molecules. To the best of our knowledge, this donor has not been used in the field of organic electroluminescent materials. The precursor **TPXZ–Br** was synthesized *via* four steps. 3,3′-oxybis(methoxybenzene), obtained from 3-iodoanisole and 3-hydroxyanisole, underwent a lithium–halogen exchange reaction to yield the key dually iodo-substituted intermediate, 3,3′-oxybis(2-iodo-1-methoxybenzene). Then, the first O- and N-bridged ring was constructed through C–N bond formations under Buchwald conditions. The pre-substituted F atoms allow for intramolecular nucleophilic substitutions, leading to the closure of the two remaining O-bridged rings. Both the target compounds were obtained as dark red powders through Ullmann coupling. Their structures were characterized by ^1H NMR spectroscopy, high-resolution mass spectrometry and elemental analysis. Thermogravimetric analysis (TGA) revealed high decomposition temperatures (T_d at 5% weight loss, Fig. S1, ESI†) of 420 and 472 °C for **TPXZ-QX** and **TPXZ-2QX** in N_2.

Single crystals of **TPXZ-QX** and **TPXZ-2QX** for X-ray diffraction studies were grown by slow evaporation of their solutions in mixed dichloromethane and hexane. The crystal data are compiled in Table S1 (ESI).† As shown in Fig. 1, the TPXZ unit in both molecules has an almost flat geometry, mainly because of the locked conformation by the three O atoms. The planarity of TPXZ is much improved compared with that of the analogue containing two O atoms (see chemical structures of **DPXZ-QX** and **DPXZ-2QX** in Fig. S2, ESI†).[20] The TPXZ and QX units in **TPXZ-QX** are arranged in a face-to-face orientation. The torsion angles of TPXZ and QX with respect to the carbazole plane are 67.6° and 67.0°, respectively. The orientation and torsion manifest the presence of strong intramolecular π–π interactions. Strikingly, the torsion angles of TPXZ and QX planes in **TPXZ-2QX** are close to 90°, revealing an ideal alignment for maximizing donor–acceptor interactions. Of note, the orthogonal orientations of the donor and acceptor with respect to the carbazolyl bridge have not been observed in previously reported molecules. This structural feature is conceived to be a result of the strong propensity to form close donor–acceptor stacks. This can be also supported by the slight bending of QX units to form a U-shaped alignment of the donor and acceptor. As expected, distances of 3.0–3.5 Å between the donor and acceptor segments are the result. It is noteworthy that the enhanced intramolecular interactions can further limit molecular vibration and rotation, which is beneficial for achieving high PLQYs (see the Theoretical calculations).
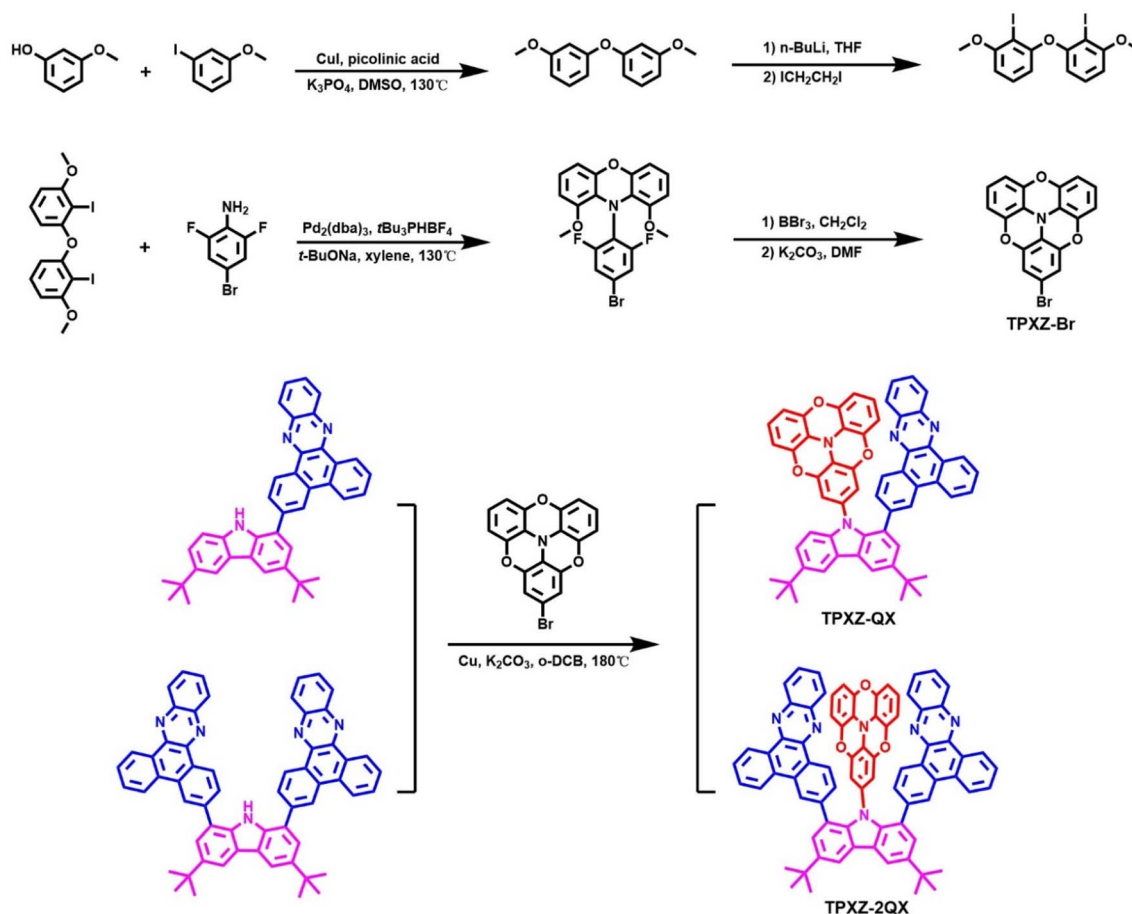
Scheme 1 Synthesis of **TPXZ-QX** and **TPXZ-2QX**.

Electrochemistry

The electrochemical properties of both compounds were examined by cyclic voltammetry in dichloromethane. As shown in Fig. 2, two quasi-reversible oxidations were observed for each compound with half-potentials ($E_{1/2}$) of 0.57/1.34 and 0.50/1.43 V *versus* Ag/AgCl, respectively. It is not unexpected that the first oxidation potentials are dominated by the TPXZ group. The HOMO energy levels of **TPXZ-QX** and **TPXZ-2QX** are estimated to be −4.88 and −4.81 eV (Table 1), respectively. Compared with **DPXZ-QX** and **DPXZ-2QX**,[20] the new compounds exhibit higher HOMO levels, which is in accordance with the electron-donating properties of the O atom. The second oxidation potentials attributable to the carbazole-centered process are nearly unaltered by the replacement of DPXZ with TPXZ. Likewise, the LUMO levels dominated by the same acceptor moieties (QX) of both compounds are almost the same as those of **DPXZ-QX** and **DPXZ-2QX**.

Photophysics

The UV-vis absorption spectra of **TPXZ-QX** and **TPXZ-2QX** were recorded in diluted toluene at room temperature. As illustrated in Fig. 3a, both compounds exhibit similar UV-vis absorption spectral profiles. The intense absorption bands below 300 nm and in the range of 350–420 nm are assigned to the typical π–π* and charge transfer (carbazole → QX) transitions, respectively. Notably, both compounds show a weak and broad absorption band in the lowest energy region from 450 to 650 nm, which is assigned to the TSCT transitions (TPXZ → QX). In particular, the TSCT absorption band of **TPXZ-2QX** is obviously stronger than that of most of the TSCT-TADF molecules.[23,33] The strong intramolecular through-space interactions brought about by the planar TPXZ unit and its close contact with the acceptor partners are conceived to interpret the enhanced TSCT intensity.

With an excitation of 400 nm, **TPXZ-QX** and **TPXZ-2QX** in diluted toluene show structure-less emission with peaks (λ_{em}) at 677 and 687 nm, respectively (Fig. 3b). With reference to previous studies on the intermediates and analogues,[20] the emissions of **TPXZ-QX** and **TPXZ-2QX** are assigned to emanate from the TSCT excited states (TPXZ → QX). Compared with **DPXZ-QX** and **DPXZ-2QX**, the emissions of **TPXZ-QX** and **TPXZ-2QX** are redshifted by 95 and 93 nm. Such large redshifts are due to the increased electron-donating capability of TPXZ and the decreased distances between the donor and acceptor(s), both of which result in strong TSCT excited states. It is worth noting that **TPXZ-QX** and **TPXZ-2QX** show single emission bands in toluene. In contrast, most of the TSCT type molecules show dual or multiple emissions from local-excitation (LE) and through-bond charge transfer states.[34,35] This distinct feature of
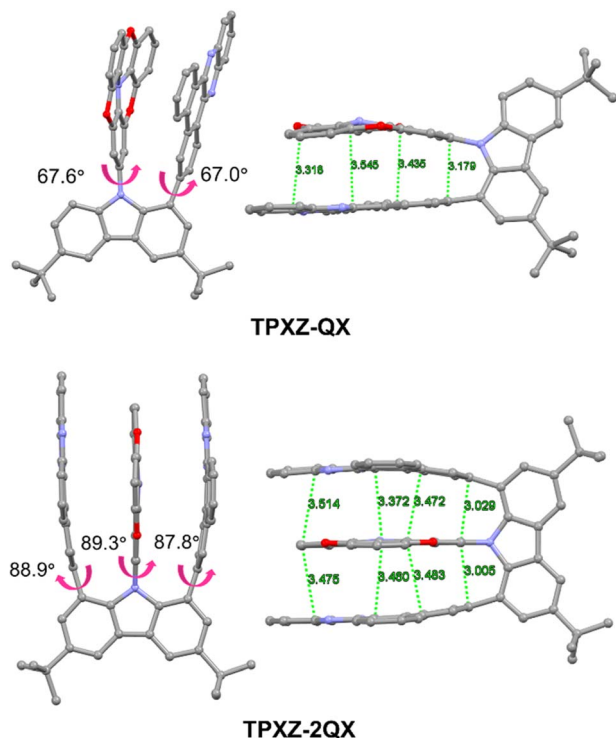
Fig. 1 Perspective views of the single crystal structures of **TPXZ-QX** and **TPXZ-2QX** with key dihedral angles and C···π/π−π distances indicated.
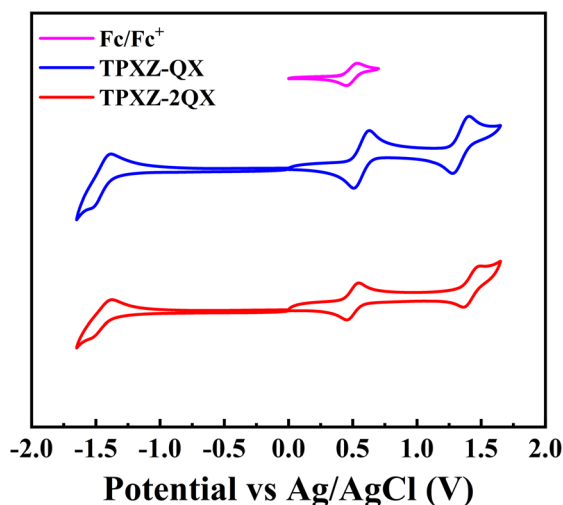

Fig. 2 Cyclic voltammograms of **TPXZ-QX** and **TPXZ-2QX** in dichloromethane with Ag/AgCl as the reference electrode. The oxidation of ferrocene occurs at $E_{1/2} = 0.49$ V.

TPXZ-QX and **TPXZ-2QX** further reveals enhanced through-space donor–acceptor interactions and thus, efficient intramolecular conversion from higher-lying local-excitation and/or through-bond charge transfer states to the TSCT state.

The solid-state emission properties of **TPXZ-QX** and **TPXZ-2QX** were studied in 5 wt% doped 9,9′-biphenyl-3,3′-diylbis-9H carbazole (mCBP) films. The relevant photophysical data are summarized in Table 1. As depicted in Fig. 4a and b, the thin

mCBP films doped with **TPXZ-QX** and **TPXZ-2QX** exhibit red to deep-red emission ($\lambda_{\mathrm{em}} = 632$ and 665 nm) at room temperature. Akin to those in toluene solutions, the emissive excited states for both compounds in the solid state are assigned as TSCT in nature. The PLQYs were determined to be 41% and 32%. As depicted in Fig. 4c and d, the transient photoluminescence characteristics of both **TPXZ-QX** and **TPXZ-2QX** show prompt and delayed decay behaviors, indicative of their TADF properties. The prompt fluorescence lifetimes (τ_{p}) of **TPXZ-QX** and **TPXZ-2QX** are 94 and 42 ns, and the delayed fluorescence lifetimes (τ_{d}) are 6.9 and 7.2 μs, respectively. Following the literature method,[36] the RISC rate constants for **TPXZ-QX** and **TPXZ-2QX** were estimated to be 1.75×10^5 and 1.53×10^5 s^{-1}, respectively (Table S2, ESI†). Of note, the nonradiative decay rate constants from S_1 to S_0 states of **TPXZ-QX** and **TPXZ-2QX** are 5.18×10^6 s^{-1} and 1.46×10^7 s^{-1}, respectively, which are much larger than those for green emitting TSCT-TADF emitters. These increases can be attributed to the energy-gap law. The phosphorescence spectra of both emitters in mCBP at 77 K were also recorded (Fig. 4a and b). Different from the vibronically structured emission profiles for **DPXZ-QX** and **DPXZ-2QX**,[20] broad and structure-less emissions were observed for **TPXZ-QX** and **TPXZ-2QX**, suggestive of their ³TSCT excited states. In addition, weak ³LE (QX) emissions at ca. 560 nm were noted for both emitters.[20] It can be seen that the emission spectra from ¹TSCT (298 K) and ³TSCT (77 K) excited states are largely overlapped, pointing to a very small ΔE_{ST}, whereas the ³TSCT phosphorescence at 77 K is slightly blueshifted comparing with the ¹TSCT fluorescence at 298 K. This energy difference is probably due to the decreased excited state structural change at 77 K. Obviously, the excited state energy diagrams account for their fast RISC processes.

Theoretical calculations

To better understand the intramolecular noncovalent interactions, the reduced density gradient (RDG) analysis based on the optimized ground-state structures is performed using the Multiwfn and VMD programs.[37–39] The gradient isosurfaces and scatter graphs of **TPXZ-QX** and **TPXZ-2QX** are shown in Fig. S3 (ESI).† In the RDG isosurfaces, the green color regions mainly appear between the TPXZ and QX segments, which reflect the presence of the π–π stacking interactions. These interactions can also be seen in RDG scatter graphs from −0.015 to 0.005 au. In addition, the intramolecular symmetry-adapted perturbation theory (I-SAPT) was used to quantitatively describe the interactions between the selected fragments.[29] The interactions between the TPXZ donor and the QX acceptor are shown in Fig. 5a and Table S3 (ESI).† In their S_0 state, the overall interactions largely stabilize **TPXZ-QX** and **TPXZ-2QX** by −15.0 and −33.1 kcal mol^{-1}, respectively. The stabilizing energies mainly stem from the dispersion interactions (−43.5 kcal mol^{-1} for **TPXZ-QX** and −93.8 kcal mol^{-1} for **TPXZ-2QX**) and electrostatic interactions (−13.0 kcal mol^{-1} for **TPXZ-QX** and −27.9 kcal mol^{-1} for **TPXZ-2QX**). The destabilizing energies are contributed by the exchange interactions. For comparison, the calculations on **DPXZ-2QX** revealed a stabilizing energy of −25.8 kcal

Table 1 Photophysical and electrochemical data of TPXZ-QX and TPXZ-2QX

Compounds	$\lambda_{em}{}^a$ (nm)	$\lambda_{em}{}^b$ (nm)	$\tau_p{}^b$ (ns)	$\tau_d{}^b$ (μs)	$\Phi_{PL}{}^b$ (%)	$E_{1/2}$(ox) (V)	E_{onset}(red) (V)	$E_{HOMO}{}^c$ (eV)	$E_{LUMO}{}^d$ (eV)
TPXZ-QX	677	632	94	6.9	41	0.57/1.34	−1.37	−4.88	−2.94
TPXZ-2QX	687	665	42	7.2	32	0.50/1.43	−1.37	−4.81	−2.94

^{a} Emission peak in toluene solution at room temperature. ^{b} Emission peak, lifetimes of prompt (τ_p) and delayed (τ_d) fluorescence, and absolute PLQY (Φ_{PL}) in 5 wt% mCBP films at room temperature in an argon atmosphere. ^{c} Estimated by using $E_{HOMO} = -e[E_{1/2}(ox) - E_{1/2}(Fc^+/Fc)] - 4.8$ eV. ^{d} Estimated by using $E_{LUMO} = -e[E_{onset}(red) - E_{1/2}(Fc^+/Fc)] - 4.8$ eV; $E_{1/2}(Fc^+/Fc) = 0.49$ eV.

mol^{-1}, which is 22% smaller than that of **TPXZ-2QX**. The stronger intramolecular interactions in **TPXZ-2QX** are mainly ascribed to the increased planarity and electron-donating capability of TPXZ. Given that the strength of noncovalent interactions is closely related to the orientation and distance of the donor–acceptor alignment, which are crucial for dictating the through-space electronic coupling,[40,41] the quantitative analysis of the stabilizing energy induced by the noncovalent interactions provides a useful clue for tuning the TSCT-TADF properties.

Density functional theory (DFT) and time-dependent DFT (TD-DFT) calculations were performed to gain deep insights into the structural and electronic properties of the ground and excited states of **TPXZ-QX** and **TPXZ-2QX**. As illustrated in Fig. S4 (ESI),† both molecules show a tilted face-to-face alignment between the donor and acceptor moieties in the ground- and excited-state geometries. It's worth noting that the π–π distances, represented by the calculated distances between the centroids of TPXZ and QX fragments at the S_0, S_1 and T_1 minima of **TPXZ-QX** and **TPXZ-2QX** (shown in Fig. 5b), are 3.0–3.5 Å, which are consistent with the crystal structures. Besides, the distance is shorter in the excited-state geometries than in the ground state geometry because the electron transition leads to enhanced intramolecular electrostatics and dispersion interactions in excited states (see Table S3, ESI†). The calculated vertical emission energies of **TPXZ-QX** and **TPXZ-2QX** are 1.81 and 1.70 eV, which are in good agreement with the experimental emission peaks of 1.83 and 1.80 eV, respectively (Table S4, ESI†). The hole and electron density distribution analyses were

performed to characterize the nature of the electronic structures of the excited states with Multiwfn and VMD packages.[42] As shown in Fig. 5c, the S_1 and T_1 states of **TPXZ-QX** and **TPXZ-2QX** show obvious TSCT character (TPXZ → QX). The T_2 state of **TPXZ-QX** is dominated by the LE of QX, while the T_2 state of **TPXZ-2QX** has a TSCT character involving a transition from TPXZ to the other QX. The small orbital overlaps of S_1 and T_1 states result in a tiny ΔE_{ST} of 0.08 eV for both **TPXZ-QX** and **TPXZ-2QX** (see Fig. 5d), which is conducive to the occurrence of TADF. Besides, to further determine whether the T_2 states participate in the luminescence, energies of the S_0, S_1, T_1 and T_2 states at the S_0, S_1 and T_1 minima are calculated. As listed in Table S5 (ESI),† considering the relaxation of excited states,[43] the T_2 state is at least 0.27 eV higher than the S_1 state at the S_1 and T_1 minima of **TPXZ-QX** and **TPXZ-2QX**. It is reasonable to preclude the thermal population of T_2 states which may mediate the RISC process. In other words, the RISC process of $T_1 \rightarrow S_1$ is the dominant channel to facilitate TADF.

Electroluminescence

Organic light-emitting devices using **TPXZ-QX** and **TPXZ-2QX** as the emitters were fabricated through vacuum deposition with an architecture of ITO/HAT-CN (5 nm)/TAPC (30 nm)/TCTA (15 nm)/mCBP (10 nm)/DMIC-TRZ:emitter (45 nm)/POT2T (20 nm)/ANT-BIZ (30 nm)/Liq (2 nm)/Al (100 nm). The energy diagram of the device and chemical structures of 1,4,5,8,9,11-hexaaza-triphenylene hexacarbonitrile (HAT-CN), di-[4-(N,N-ditolyl-amino)-phenyl]cyclohexane (TAPC), 4,4′4″-tris(carbazole-9-yl)
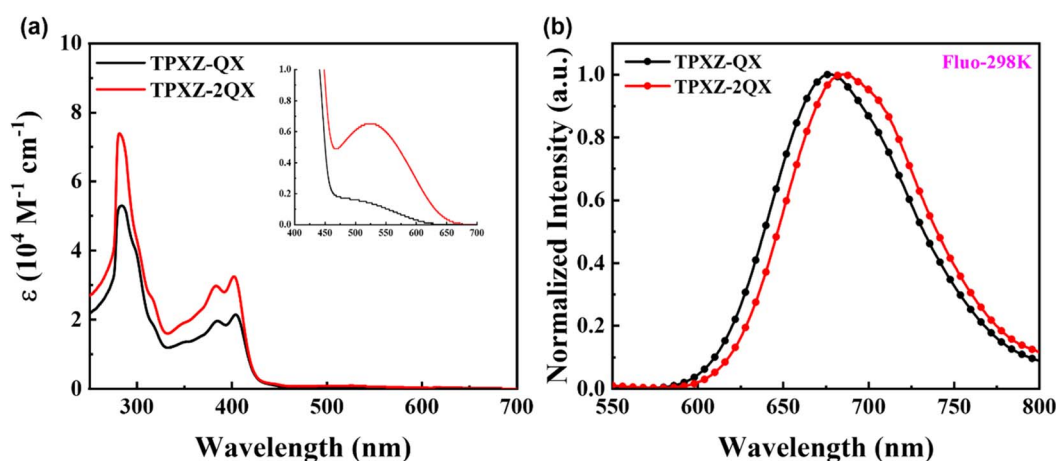

Fig. 3 (a) UV-vis absorption and (b) fluorescence spectra ($\lambda_{ex} = 400$ nm) of **TPXZ-QX** and **TPXZ-2QX** in dilute toluene at 298 K.
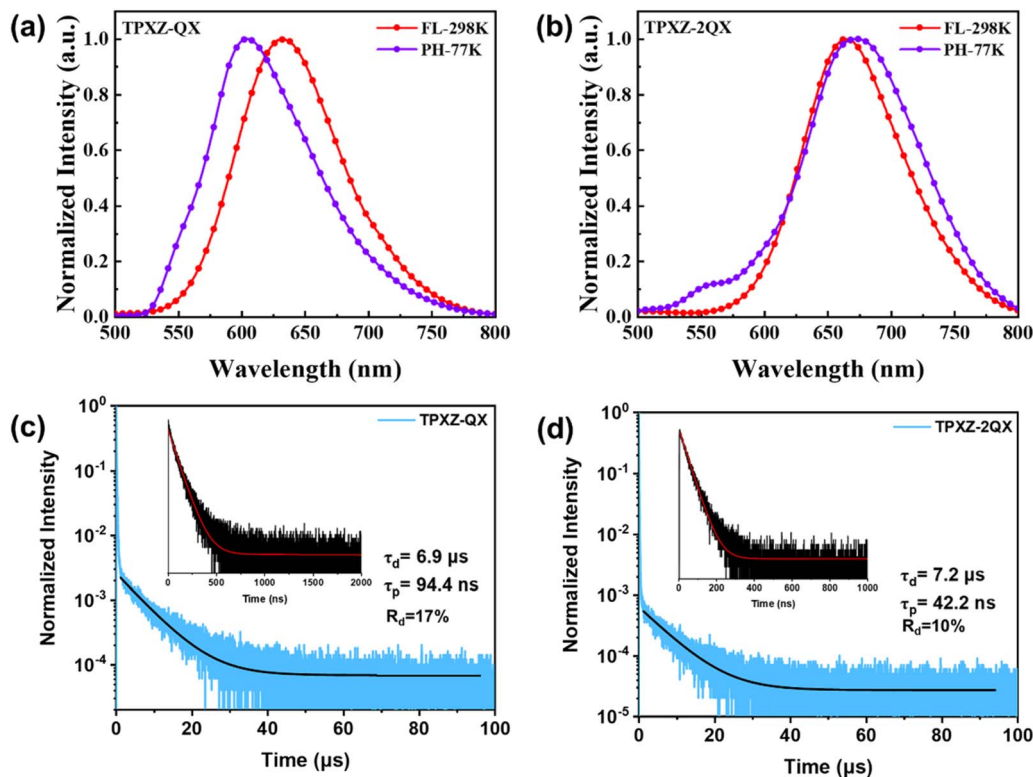
Fig. 4 (a and b) Photoluminescence spectra and (c and d) transient characteristics of **TPXZ–QX** and **TPXZ–2QX** in doped mCBP films (5 wt%). R_d represents the ratio of the delayed fluorescence component.

triphenylamine (TCTA), mCBP, 1,3-dihydro-1,1-dimethyl-3-(3-(4,6-diphenyl-1,3,5-triazin-2-yl)phenyl)indeno-[2,1-*b*]carbazole (DMIC-TRZ), (1,3,5-triazine-2,4,6-triyl)tris(benzene-3,1-diyl) tris(diphenyl-phosphine oxide) (POT2T), and 1-[4-(10-[1,1′-

biphenyl]-4-yl-9-anthracenyl)phenyl]-2-ethyl-1*H*-benzimidazole (ANT-BIZ) are depicted in Fig. S5 (ESI).† DMIC-TRZ was used as the host material.
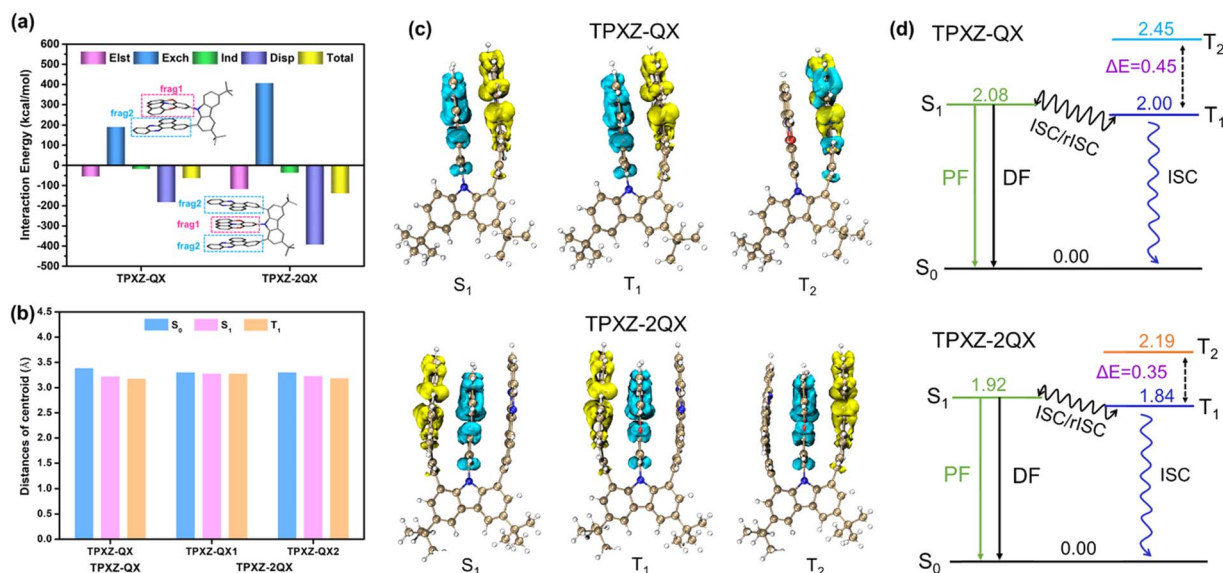

Fig. 5 (a) Electronic interactions between selected fragments in **TPXZ–QX** and **TPXZ–2QX** by the I–SAPT approach. (b) Calculated distances between the centroids of TPXZ and QX fragments at the S_0, S_1 and T_1 minima of **TPXZ–QX** and **TPXZ–2QX**. (c) Calculated hole (blue) and electron (yellow) distributions and (d) possible luminescence mechanisms of **TPXZ–QX** and **TPXZ–2QX**. S_1 and T_1 states are analyzed at their minima, respectively, while T_2 states are analyzed at the T_1 minima.
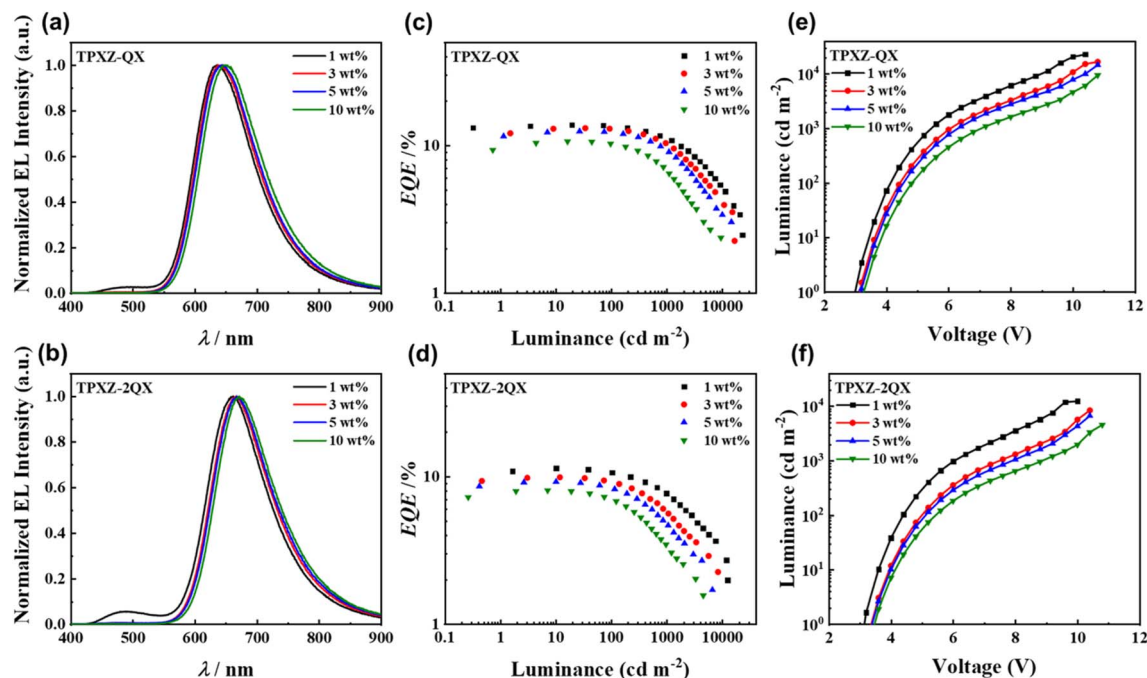
Fig. 6 Device characteristics based on **TPXZ-QX** and **TPXZ-2QX**. (a and b) Electroluminescence (EL) spectra of the devices. (c and d) The EQE–luminance curves of the devices. (e and f) Luminance–voltage curves of the devices.

Device characteristics are plotted in Fig. 6 and S6 (ESI).† The key numerical device data are compiled in Table 2. The electroluminescence (EL) maxima are located at 637–649 nm and 662–672 nm for **TPXZ-QX** and **TPXZ-2QX**, respectively, dependent on the dopant concentration. In line with their photoluminescence difference, the electroluminescence spectra of the devices based on **TPXZ-2QX** are redshifted by 20–30 nm from those of **TPXZ-QX**. For both emitters, the 1 wt%-doped devices show the maximum EQE/current efficiency/power efficiency, which were obtained as 13.8%/11.2 cd A^{-1}/9.7 lm W^{-1} and 11.4%/4.9 cd A^{-1}/4.3 lm W^{-1}, respectively, which are the highest among all the dopant concentrations. The peak luminance values are 22 800 and 12 300 cd m^{-2}. It is noted that there is residual host emission for the devices with 1 wt% dopant

concentration. On increasing dopant concentration to 3 wt%, the host emission was completely attenuated, giving rise to improved chromaticity with a CIEx of 0.65 for **TPXZ-QX** and 0.67 for **TPXZ-2QX** (Table 2). In the meantime, the device efficiencies were found to decrease as the dopant concentration increases. In addition to the possible concentration quenching effect, it is speculated that the emitter acts as a trapping center for charge carriers, which may result in unbalanced charge transport. This can be supported by the decreased current density when the dopant concentration is higher (Fig. S6, ESI†). The occurrence of charge trapping can further be manifested by using the photoluminescence spectra of **TPXZ-QX** and **TPXZ-2QX** in DMIC-TRZ with a dopant level of 3 wt%. As shown in Fig. S7,† in addition to the dopant emissions with a λ_{em} of 630 and 656 nm,

Table 2 Summary of key device data based on **TPXZ-QX** and **TPXZ-2QX**

Conc.	L^a [cd m^{-2}]	CE^b [cd A^{-1}]	PE^b [lm W^{-1}]	EQE^b [%]	λ_{max}^c [nm]	CIE^c [(x, y)]
TPXZ-QX						
1 wt%	22 800	11.2; 10.3	9.7; 6.2	13.8; 11.7	637	0.63, 0.36
3 wt%	16 600	9.6; 8.1	7.6; 4.3	13.1; 10.4	643	0.65, 0.35
5 wt%	14 600	8.4; 6.6	6.6; 3.2	12.5; 9.1	646	0.65, 0.35
10 wt%	9400	5.8; 4.0	4.6; 1.8	10.7; 6.5	649	0.66; 0.34
TPXZ-2QX						
1 wt%	12 300	4.9; 4.1	4.3; 2.1	11.4; 7.7	662	0.61, 0.34
3 wt%	8400	3.4; 2.2	2.6; 0.9	9.9; 5.6	667	0.67, 0.32
5 wt%	6600	2.8; 1.6	2.2; 0.7	9.2; 4.7	668	0.67, 0.32
10 wt%	4500	2.0; 1.0	1.6; 0.4	8.1; 3.5	672	0.68, 0.31

^{a} Maximum luminance. ^{b} Values of current efficiency (CE), power efficiency (PE), and external quantum efficiency (EQE) at the maximum and 1000 cd m^{-2}. ^{c} λ_{max} and CIE coordinates at 1000 cd m^{-2}.

intense host fluorescent emissions at *ca.* 500 nm are also evident. The much lower relative intensities of the host emission in electroluminescence spectra than in photoluminescence spectra reveal that the emitters can be electrically excited directly in operating devices. The TADF activity of **TPXZ-QX** and **TPXZ-2QX** in DMIC-TRZ films was corroborated by transient photoluminescence measurements at varying temperatures from 77 K to 300 K (Fig. S8, ESI†). The τ_d was determined to be 7.9 and 7.8 μs for **TPXZ-QX** and **TPXZ-2QX** (Fig. S7, ESI†), respectively, which are comparable to those in mCBP films. As summarized in Table S6,† an EQE_{max} of 11.4% for **TPXZ-2QX** represents one of the most efficient TSCT-TADF devices with an electroluminescence peak beyond 650 nm. Compared with deep-red electroluminescence based on a through bond charge transfer process, **TPXZ-2QX** is still a rare example. Therefore, the TPXZ donor featuring a flat and rigid structure provides a new choice for the design of long-wavelength TADF emitters.

Conclusions

In summary, two red and deep-red TSCT-TADF emitters have been designed and synthesized. Oxygen-bridged triphenylamine (TPXZ), which has a flat and rigid geometry and strong electron-donating capability, was used as the donor. The alignment of the donor and planar acceptor(s) in a face-to-face orientation allows for strong intramolecular donor–acceptor stacking interactions. Theoretical investigation of the noncovalent interactions unveiled the major contributions of the dispersion and electrostatic interactions to the overall stabilizing energy. The emitters show moderate photoluminescence quantum yields of up to 41% and short TADF lifetimes (<8 μs) in doped thin films. Maximum EQE values of up to 13.8% and 11.4% for red (637 nm) and deep-red (662 nm) electroluminescence were achieved, respectively. This study provides a molecular design for the development of high-efficiency long-wavelength emitters and devices.

Data availability

All data supporting the findings of this study are presented in the article and ESI.† Additional data are available from the corresponding author upon reasonable request.

Author contributions

X.-F. Song and C. Jiang synthesized the molecules, carried out the photophysical measurements and theoretical calculations, and wrote the manuscript draft. N. Li and J. Miao performed the fabrications and characterization studies of the OLEDs. K. Li and C. Yang conceived the idea, designed the experiments, and wrote the manuscript. K. Li and C. Yang supervised this study.

Conflicts of interest

There are no conflicts to declare.

References

1 H. Uoyama, K. Goushi, K. Shizu, H. Nomura and C. Adachi, *Nature*, 2012, **492**, 234–238.

2 K. Goushi, K. Yoshida, K. Sato and C. Adachi, *Nat. Photonics*, 2012, **6**, 253–258.

3 Q. S. Zhang, J. Li, K. Shizu, S. P. Huang, S. Hirata, H. Miyazaki and C. Adachi, *J. Am. Chem. Soc.*, 2012, **134**, 14706–14709.

4 G. Mehes, H. Nomura, Q. S. Zhang, T. Nakagawa and C. Adachi, *Angew. Chem., Int. Ed.*, 2012, **51**, 11311–11315.

5 D. D. Zhang, L. Duan, C. Li, Y. L. Li, H. Y. Li, D. Q. Zhang and Y. Qiu, *Adv. Mater.*, 2014, **26**, 5050–5055.

6 T. J. Penfold, E. Gindensperger, C. Daniel and C. M. Marian, *Chem. Rev.*, 2018, **118**, 6975–7025.

7 Q. Peng, D. Fan, R. H. Duan, Y. P. Yi, Y. L. Niu, D. Wang and Z. G. Shuai, *J. Phys. Chem. C*, 2017, **121**, 13448–13456.

8 P. K. Samanta, D. Kim, V. Coropceanu and J. L. Bredas, *J. Am. Chem. Soc.*, 2017, **139**, 4042–4051.

9 Z. Yang, Z. Mao, Z. Xie, Y. Zhang, S. Liu, J. Zhao, J. Xu, Z. Chi and M. P. Aldred, *Chem. Soc. Rev.*, 2017, **46**, 915–1016.

10 Y. Geng, A. D'Aleo, K. Inada, L. S. Cui, J. U. Kim, H. Nakanotani and C. Adachi, *Angew. Chem., Int. Ed.*, 2017, **56**, 16536–16540.

11 S. Shao, J. Hu, X. Wang, L. Wang, X. Jing and F. Wang, *J. Am. Chem. Soc.*, 2017, **139**, 17739–17742.

12 H. Tsujimoto, D.-G. Ha, G. Markopoulos, H. S. Chae, M. A. Baldo and T. M. Swager, *J. Am. Chem. Soc.*, 2017, **139**, 4894–4900.

13 X.-Q. Wang, S.-Y. Yang, Q.-S. Tian, C. Zhong, Y.-K. Qu, Y.-J. Yu, Z.-Q. Jiang and L.-S. Liao, *Angew. Chem., Int. Ed.*, 2021, **60**, 5213–5219.

14 X. Tang, L.-S. Cui, H.-C. Li, A. J. Gillett, F. Auras, Y.-K. Qu, C. Zhong, S. T. E. Jones, Z.-Q. Jiang, R. H. Friend and L.-S. Liao, *Nat. Mater.*, 2020, **19**, 1332–1338.

15 Z.-Q. Feng, S.-Y. Yang, F.-C. Kong, Y.-K. Qu, X.-Y. Meng, Y.-J. Yu, D.-Y. Zhou, Z.-Q. Jiang and L.-S. Liao, *Adv. Funct. Mater.*, 2023, **33**, 2209708.

16 X. Wang, S. Wang, J. Lv, S. Shao, L. Wang, X. Jing and F. Wang, *Chem. Sci.*, 2019, **10**, 2915–2923.

17 X. Wang, J. Hu, J. Lv, Q. Yang, H. Tian, S. Shao, L. Wang, X. Jing and F. Wang, *Angew. Chem., Int. Ed.*, 2021, **60**, 16585–16593.

18 C. Wu, W. Liu, K. Li, G. Cheng, J. Xiong, T. Teng, C.-M. Che and C. Yang, *Angew. Chem., Int. Ed.*, 2021, **60**, 3994–3998.

19 J. Wang, J. Miao, C. Jiang, S. Luo, C. Yang and K. Li, *Adv. Opt. Mater.*, 2022, **10**, 202201071.

20 C. Jiang, J. Miao, D. Zhang, Z. Wen, C. Yang and K. Li, *Research*, 2022, **2022**, 9892802.

21 T. Huang, Q. Wang, G. Meng, L. Duan and D. Zhang, *Angew. Chem., Int. Ed.*, 2022, **61**, e202200059.

22 F.-M. Xie, H.-Z. Li, K. Zhang, Y. Shen, X. Zhao, Y.-Q. Li and J.-X. Tang, *Angew. Chem., Int. Ed.*, 2022, **61**, e202213823.

23 Y. J. Song, Y. B. Li, R. Y. Yu, K. Zhang and L. He, *Adv. Opt. Mater.*, 2023, 202300432.

24 S. L. Liu, Q. W. Li, L. Hua, Z. N. Zhao, Z. J. Ren and S. K. Yan, *Macromol. Rapid Commun.*, 2022, **43**, 202200064.

25 Y. J. Song, M. X. Tian, R. Y. Yu and L. He, *ACS Appl. Mater. Interfaces*, 2021, **13**, 60269–60278.

26 Z. N. Zhao, C. Zeng, X. M. Peng, Y. C. Liu, H. S. Zhao, L. Hua, S. J. Su, S. K. Yan and Z. J. Ren, *Angew. Chem., Int. Ed.*, 2022, **61**, e202210864.

27 J. Hu, Q. Li, X. Wang, S. Shao, L. Wang, X. Jing and F. Wang, *Angew. Chem., Int. Ed.*, 2019, **58**, 8405–8409.

28 X. Wang, J. Hu, J. Lv, Q. Yang, H. Tian, S. Shao, L. Wang, X. Jing and F. Wang, *Angew. Chem., Int. Ed.*, 2021, **60**, 16585–16593.

29 R. M. Parrish, J. F. Gonthier, C. Corminboeuf and C. D. Sherrill, *J. Chem. Phys.*, 2015, **143**, 051103.

30 J. M. Turney, A. C. Simmonett, R. M. Parrish, E. G. Hohenstein, F. A. Evangelista, J. T. Fermann, B. J. Mintz, L. A. Burns, J. J. Wilke, M. L. Abrams, N. J. Russ, M. L. Leininger, C. L. Janssen, E. T. Seidl, W. D. Allen, H. F. Schaefer, R. A. King, E. F. Valeev, C. D. Sherrill and T. D. Crawford, *Wiley Interdiscip. Rev.: Comput. Mol. Sci.*, 2012, **2**, 556–565.

31 M. Kuratsu, M. Kozaki and K. Okada, *Angew. Chem., Int. Ed.*, 2005, **44**, 4056–4058.

32 S. Breimaier and R. F. Winter, *Eur. J. Org Chem.*, 2021, **2021**, 4690–4700.

33 M. Yu, X. Zhu, J. Zeng, H. Liu, R. Huang, Z. Zhuang, P. Shen, Z. Zhao and B. Z. Tang, *J. Mater. Chem. C*, 2021, **9**, 14808–14814.

34 X. Zheng, R. Huang, C. Zhong, G. Xie, W. Ning, M. Huang, F. Ni, F. B. Dias and C. Yang, *Adv. Sci.*, 2020, **7**, e202210864.

35 Q. Li, Y. Wu, J. Cao, Y. Liu, Z. Wang, H. Zhu, H. Zhang and F. Huang, *Angew. Chem., Int. Ed.*, 2022, **61**, e202202381.

36 K.-C. Pan, S.-W. Li, Y.-Y. Ho, Y.-J. Shiu, W.-L. Tsai, M. Jiao, W.-K. Lee, C.-C. Wu, C.-L. Chung, T. Chatterjee, Y.-S. Li, K.-T. Wong, H.-C. Hu, C.-C. Chen and M.-T. Lee, *Adv. Funct. Mater.*, 2016, **26**, 7560–7571.

37 E. R. Johnson, S. Keinan, P. Mori-Sánchez, J. Contreras-García, A. J. Cohen and W. Yang, *J. Am. Chem. Soc.*, 2010, **132**, 6498–6506.

38 T. Lu and F. Chen, *J. Comput. Chem.*, 2012, **33**, 580–592.

39 W. Humphrey, A. Dalke and K. Schulten, *J. Mol. Graph.*, 1996, **14**, 33–38.

40 Y. K. Kang, P. Zhang, I. V. Rubtsov, J. Zheng, G. Bullard, D. N. Beratan and M. J. Therien, *J. Phys. Chem. B*, 2019, **123**, 10456–10462.

41 H. W. Jung, S. E. Yoon, P. J. Carroll, M. R. Gau, M. J. Therien and Y. K. Kang, *J. Phys. Chem. B*, 2020, **124**, 1033–1048.

42 Z. Liu, T. Lu and Q. Chen, *Carbon*, 2020, **165**, 461–467.

43 X.-F. Song, Z.-W. Li, W.-K. Chen, Y.-J. Gao and G. L. Cui, *Inorg. Chem.*, 2022, **61**, 7673–7681.